

# Spin-orbit-entangled state of $\text{Ba}_2\text{CaOsO}_6$ studied by O $K$ -edge resonant inelastic X-ray scattering and Raman spectroscopy

J. Okamoto,<sup>1</sup> G. Shibata,<sup>2</sup> Yu. S. Ponosov,<sup>3</sup> H. Hayashi,<sup>4,5,\*</sup> K. Yamaura,<sup>4,5</sup> H. Y. Huang,<sup>1</sup> A. Singh,<sup>1</sup> C. T. Chen,<sup>1</sup> A. Tanaka,<sup>6</sup> S. V. Streltsov,<sup>3,7,†</sup> D. J. Huang,<sup>1,8,9,‡</sup> and A. Fujimori<sup>1,2,10,11,§</sup>

<sup>1</sup>National Synchrotron Radiation Research Center, Hsinchu 300092, Taiwan

<sup>2</sup>Materials Sciences Research Center, Japan Atomic Energy Agency, Sayo, Hyogo 679-5148, Japan

<sup>3</sup>Institute of Metal Physics, 620041 Ekaterinburg GSP-170, Russia

<sup>4</sup>Research Center for Materials Nanoarchitectonics (MANA),

National Institute for Materials Science, Tsukuba, Ibaraki 305-0044, Japan

<sup>5</sup>Graduate School of Chemical Sciences and Engineering,

Hokkaido University, Sapporo, Hokkaido 060-0810, Japan

<sup>6</sup>Department of Quantum Matter, Hiroshima University, Hiroshima 739-8530, Japan

<sup>7</sup>Department of Theoretical Physics and Applied Mathematics,

Ural Federal University, 620002 Ekaterinburg, Russia

<sup>8</sup>Department of Physics, National Tsing Hua University, Hsinchu 300044, Taiwan

<sup>9</sup>Department of Electrophysics, National Yang Ming Chiao Tung University, Hsinchu 300093, Taiwan

<sup>10</sup>Center for Quantum Science and Technology and Department of Physics,

National Tsing Hua University, Hsinchu 300044, Taiwan

<sup>11</sup>Department of Physics, The University of Tokyo, Bunkyo-Ku, Tokyo 113-0033, Japan

(Dated: February 26, 2025)

Transition-metal ions with  $5d^2$  electronic configuration in a cubic crystal field are prone to have a vanishing dipolar magnetic moment but finite higher-order multipolar moments, and they are expected to exhibit exotic physical properties. Through an investigation using resonant inelastic X-ray scattering (RIXS), Raman spectroscopy, and theoretical ligand-field (LF) multiplet and *ab initio* calculations, we fully characterized the local electronic structure of  $\text{Ba}_2\text{CaOsO}_6$ , particularly, the crystal-field symmetry of the  $5d^2$  electrons in this anomalous material. The low-energy multiplet excitations from RIXS at the oxygen  $K$  edge and Raman-active phonons both show no splitting. These findings are consistent with the ground state of Os ions dominated by magnetic octupoles. Obtained parameters pave the way for further realistic microscopic studies of this highly unusual class of materials, advancing our understanding of spin-orbit physics in systems with higher-order multipoles.

## I. INTRODUCTION

$5d$  transition-metal oxides exhibit various exotic physical properties arising from the strong spin-orbit coupling (SOC) that competes with Hund's coupling and Jahn-Teller effect and strongly influences the exchange interaction [1–3]. Particularly attractive have been the Mott-insulating  $\text{Ir}^{4+}$  ( $5d^5$ ) compounds with effective angular momentum  $J_{\text{eff}} = 1/2$  and the Kitaev quantum-spin-liquid candidate of  $\text{Ru}^{3+}$  ( $4d^5$ ) honeycomb lattices. Especially exotic are localized  $5d^2$  electrons in a cubic crystal field. A  $d^2$  ion coordinated by ligand atoms in the octahedral ( $O_h$ ) environment is expected to be Jahn-Teller active, but many cubic crystals with  $5d^2$  ions remain undistorted, probably due to the strong SOC of the  $5d$  electrons [4]. Such a  $5d^2$  ion in the  $O_h$ -symmetry crystal field has a non-Kramers doublet ground state that supports either an electric quadrupole or a magnetic oc-

tupole [5–9]. This is contrasted with  $5d^1$  systems, where the  $5d$  ion has an electric quadrupole and Jahn-Teller distortion is induced [1, 2, 4, 7, 10]. As a staggered octupolar order has been predicted theoretically for quarter-filled manganites [11], one may conceive disordered octupoles or a quantum octupole liquid under particular conditions in manganites or other materials.

The  $B$ -site-ordered double perovskite  $\text{Ba}_2\text{AOsO}_6$ , where  $A$  is an alkali-earth metal, is one of such  $5d^2$  ( $\text{Os}^{6+}$ ) systems. The face-centered cubic (fcc) lattice formed by the Os ions may induce geometrical frustrations between the multipoles, and may lead to intriguing quantum magnetism predicted theoretically [5–9]. For example,  $\text{Ba}_2\text{CaOsO}_6$  shows a cusp-like anomaly in the magnetic susceptibility at  $T^* \sim 50$  K, signaling a magnetic transition, and muon-spin rotation ( $\mu$ -SR) has revealed a small magnetic moment of  $\sim 0.2 \mu_B$  [12] or  $\sim 0.05 \mu_B$  per Os ion [13] whereas neutron scattering has detected no magnetic Bragg peaks below  $T^*$  [12]. (According to Ref.[13], the small magnetic moment may be induced by impurities and may not be intrinsic.) According to X-ray diffraction, the crystal remains cubic down to the lowest temperatures [14]. This precludes static electric quadrupolar order, which should distort the cubic lattice [10], but is consistent with magnetic octupolar order as the origin of the ‘hidden order’ in  $\text{Ba}_2\text{AOsO}_6$ . Theo-

\* present address: *Institute for Solid State Physics, The University of Tokyo, 5-1-5 Kashiwanoha, Kashiwa, Chiba 277-8581, Japan*

† email: [streltsov@imp.uran.ru](mailto:streltsov@imp.uran.ru)

‡ email: [djhuang@nsrrc.org.tw](mailto:djhuang@nsrrc.org.tw)

§ email: [fujimori@phys.s.u-tokyo.ac.jp](mailto:fujimori@phys.s.u-tokyo.ac.jp)

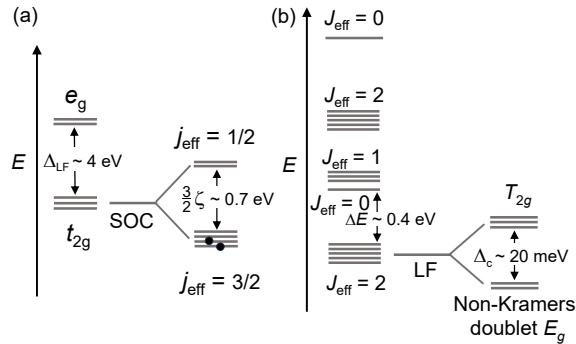


FIG. 1. Energy diagrams of the  $\text{Os}^{6+}$  ( $5d^2$ ) ion in the cubic ( $O_h$ ) crystal field. (a) One-electron energy diagram.  $\Delta_{\text{LF}}$  is the  $t_{2g}$ - $e_g$  splitting. Spin-orbit coupling (SOC) further splits the  $t_{2g}$  level into  $j_{\text{eff}} = \frac{1}{2}$  and  $j_{\text{eff}} = \frac{3}{2}$  levels separated by  $\frac{3}{2}\zeta$ , and the  $j_{\text{eff}} = \frac{3}{2}$  level is occupied by two electrons. (b) Two-electron energy diagram. The  $t_{2g}^2$  part of the  $d^2$  multiplet is shown whereas the  $t_{2g}e_g$  part is located at higher energies separated by  $\sim \Delta_{\text{LF}}$ . Due to the ligand field (LF) of cubic symmetry, the  $J_{\text{eff}} = 2$  ground state is split by a ‘residual’ cubic splitting  $\Delta_c$  into the non-Kramers  $E_g$  doublet and the  $T_{2g}$  triplet. The first  $J_{\text{eff}} = 0$  excited state appears  $\Delta E \sim 0.4$  eV above the ground state, and the first  $J_{\text{eff}} = 1$  excited state  $\sim 0.065$  eV above it.

retically, exchange coupling between neighboring Os ions favors ferro-octupolar order in the fcc lattice [6].

In an  $O_h$ -symmetry crystal field, the one-electron  $5d$  level is split into the  $t_{2g}$  and  $e_g$  levels separated by  $\Delta_{\text{LF}}$  [Fig. 1(a)]. The strong SOC splits the  $t_{2g}$  level into the  $j_{\text{eff}} = \frac{1}{2}$  and  $j_{\text{eff}} = \frac{3}{2}$  sublevels, and the latter is occupied by the two electrons of the  $\text{Os}^{6+}$  ion. In the two-electron energy diagram [Fig. 1(b)], the ground state has the total effective angular momentum of  $J_{\text{eff}} = 2$ . Under the  $O_h$  symmetry, the ‘residual’ cubic crystal-field splits the  $J_{\text{eff}} = 2$  quintet into the ground-state  $E_g$  doublet and the triply-degenerate  $T_{2g}$  excited states with a separation  $\Delta_c$  [14, 15]. The  $E_g$  ground state is a non-Kramers doublet consisting of  $|\psi_{g,\uparrow}\rangle \equiv |J_{\text{eff}}^z = 0\rangle$  and  $|\psi_{g,\downarrow}\rangle \equiv \frac{1}{\sqrt{2}}(|J_{\text{eff}}^z = 2\rangle + |J_{\text{eff}}^z = -2\rangle)$ , whereas the  $T_{2g}$  excited states consist of  $|\psi_{e,\pm}\rangle \equiv |J_{\text{eff}}^z = \pm 1\rangle$  and  $|\psi_{e,0}\rangle \equiv \frac{1}{\sqrt{2}}(|J_{\text{eff}}^z = 2\rangle - |J_{\text{eff}}^z = -2\rangle)$ . In the ferro-octupole-ordered state, all the Os ions are in one of the two eigenstates,  $|\psi_{g,\pm}\rangle \equiv \frac{1}{\sqrt{2}}(|\psi_{g,\uparrow}\rangle \pm i|\psi_{g,\downarrow}\rangle)$ , of the octupole operator  $T_{xyz} \propto \overline{J^x J^y J^z}$ , where the overline denotes symmetrization.

While the magnetic properties of  $\text{Ba}_2\text{AOsO}_6$  double perovskites have been widely studied and microscopic models to explain observed anomalies have been proposed, their electronic structure remains unexplored experimentally. The present paper aims to fill this gap. In particular, we studied  $\text{Ba}_2\text{CaOsO}_6$  by X-ray absorp-

tion spectroscopy (XAS) and resonant inelastic X-ray scattering (RIXS) at the O  $K$  edge. RIXS studies of  $5d$  transition-metal oxides have so far been performed mainly at the transition-metal  $L_{2,3}$  edge since one can directly study the spin and orbital excitation of the  $5d$  states [16–19]. However, owing to the strong SOC of the  $5d$  electrons, RIXS at the O  $K$  edge can also be used to study spin excitations [Fig. 1(b)] [20–24]. O  $K$ -edge RIXS has the advantage of having higher energy resolution than transition-metal  $L_{2,3}$ -edge RIXS, allowing us to study low-energy electronic excitation and electron-phonon interaction. We have also utilized Raman scattering to detect possible local lattice distortion that induces low-symmetry crystal fields. None of the above measurements have indeed shown evidence for the lowering of the cubic symmetry, favoring the scenario that the Os ions have dominantly octupolar moments in  $\text{Ba}_2\text{CaOsO}_6$ .

## II. RESULTS AND ANALYSES

We performed O  $K$ -edge RIXS on high-quality polycrystalline samples with the energy resolution of  $\sim 30$  meV using  $\pi$  polarized X-rays and  $90^\circ$  scattering angle (see Methods). The O  $K$ -edge XAS spectrum is shown in Fig. 2(a). Figure 2(b) shows the RIXS intensity map in the  $E_{\text{in}}-E_{\text{loss}}$  plane, where  $E_{\text{in}}$  is the energy of incident X-ray and  $E_{\text{loss}}$  is the energy loss of scattered X-rays. The same data are plotted in the  $E_{\text{in}}-E_{\text{em}}$  plane in Fig. 2(c), where  $E_{\text{em}}$  is the energy of emitted X-ray. RIXS spectra are plotted in Fig. 2(d). In the figure, above  $E_{\text{in}} \sim 529$  eV, some spectral features start to shift to higher  $E_{\text{loss}}$  with increasing  $E_{\text{in}}$ , indicating a cross-over from Raman-like to fluorescence-like.

### Splitting due to ligand field and spin-orbit coupling

In O  $K$ -edge RIXS, the excitation of the O  $1s$  core electron into empty states followed by the electron transition from the non-bonding O  $2p$  band to the O  $1s$  core level leaves a hole in the non-bonding O  $2p$  band and an electron in the empty states. The resulting final state is equivalent to that of the O  $2p \rightarrow \text{Os } 5d$  charge-transfer (CT) excitation, which measures the unoccupied part of the O  $2p$  partial density of states (PDOS). Because the energy position of the non-bonding O  $2p$  band is located near the top of the O  $2p$  band, we assumed it located  $\sim 2$  eV below the Fermi level ( $E_F$ ), based on the occupied O  $2p$  PDOS deduced from fluorescence spectra as discussed below. Thus one finds the  $e_g$  band 4-6 eV above  $E_F$ , the  $j_{\text{eff}} = \frac{1}{2}$  band  $\sim 1$  eV above  $E_F$ , the empty and occupied parts of the  $j_{\text{eff}} = \frac{3}{2}$  band just above and below  $E_F$ , respectively.

The occupied part of the O  $2p$  PDOS can be measured by the fluorescence component of the O  $K$ -edge RIXS. We have taken spectrum k in Fig. 2(d) as the representative fluorescence spectrum. The  $E_F$  position for the

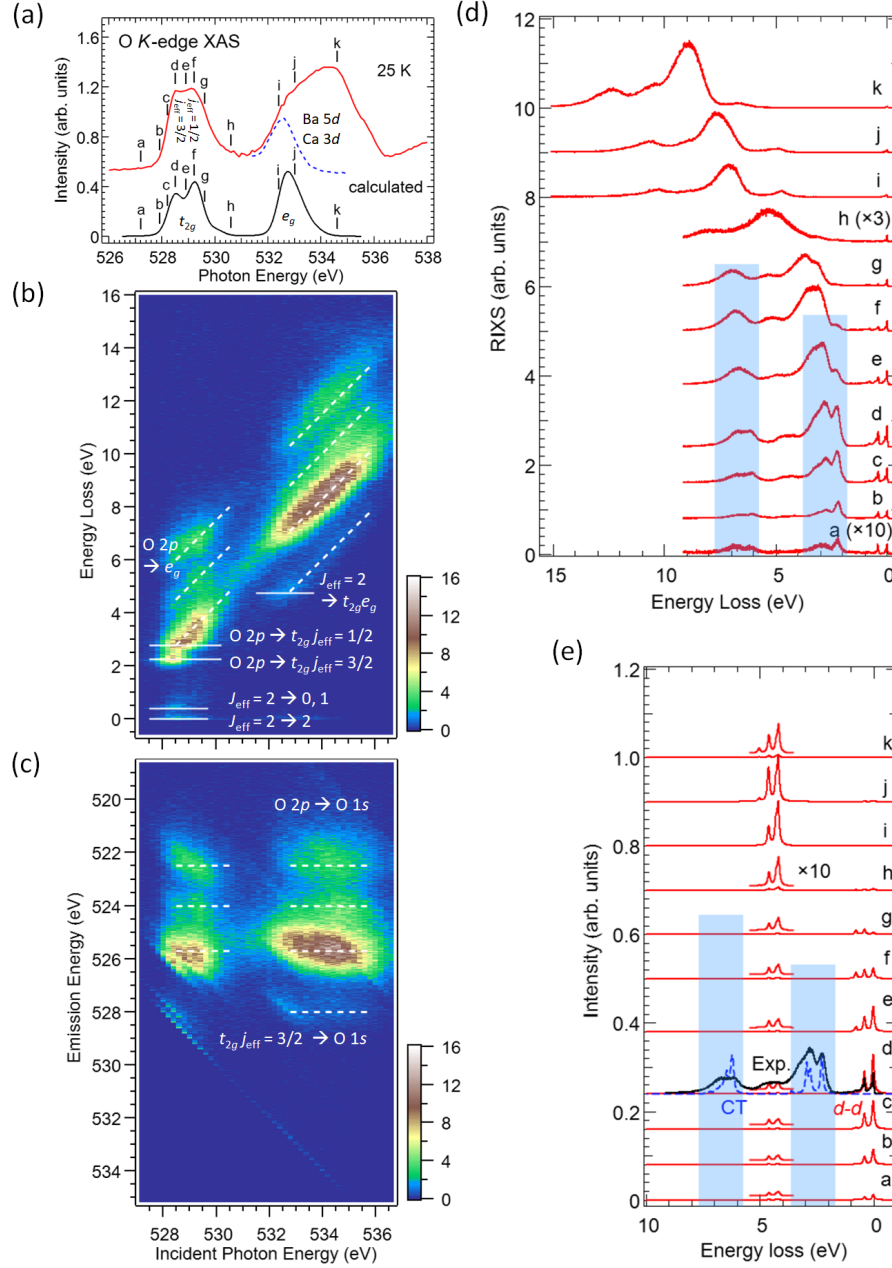


FIG. 2. X-ray absorption spectroscopy (XAS) and resonant inelastic X-ray scattering (RIXS) spectra of  $\text{Ba}_2\text{CaOsO}_6$  at the oxygen  $K$  edge recorded at 25 K. (a) XAS spectra. Top: XAS spectrum measured using the total fluorescence-yield method. The broad absorption band at 532-536 eV consists of transitions to the empty  $e_g$  states (blue dashed curve) as well as to the Ba  $5d$ - and Ca  $3d$ -derived conduction-band states. The blue dashed curve is the partial fluorescence-yield spectrum measured at  $E_{\text{em}} = 528$  eV. Bottom: Spectrum calculated using ligand-field (LF) multiplet theory. See Methods. (b) & (c) Colored intensity maps of scattered X-rays: (b) as a function of incident X-ray energy  $E_{\text{in}}$  and energy loss  $E_{\text{loss}}$ . Solid lines mark the positions of constant  $E_{\text{loss}}$ . Dashed lines indicate those of constant  $E_{\text{em}}$ , (c) Scattered X-ray intensity map plotted against  $E_{\text{in}}$  and emission energy  $E_{\text{em}}$ . Dashed lines indicate constant  $E_{\text{em}}$ 's, corresponding to fluorescence from occupied states to the O  $1s$  core level. (d) RIXS spectra measured for various  $E_{\text{in}}$ 's indicated by vertical bars at the top spectrum of (a). The shaded parts mark transitions from  $\text{O } 2p \rightarrow \text{Os } 5d$  charge-transfer (CT) excitation. (e) LF multiplet calculation to simulate the RIXS spectra. The red curves show spectra arising from  $d-d$  excitation for a series of  $E_{\text{in}}$ 's indicated by vertical bars in the calculated O  $K$ -edge XAS spectrum shown at the bottom of (a). The dashed blue curves show  $\text{O } 2p \rightarrow \text{Os } 5d$  CT excitation simulated by  $5d^2 \rightarrow 5d^3$  multiplet calculation. The black curve is the measured RIXS spectrum for  $E_{\text{in}} = 528.5$  eV [spectrum d in panel (d)].

143 fluorescence spectrum has been fixed under the assumption  
 144 that  $E_{\text{em}} = 528.2$  eV is the excitation threshold of  
 145 the O  $K$ -edge XAS [photon energy  $c$  in Fig. 2(a)]. The  
 146 combined occupied and unoccupied parts of the O  $2p$   
 147 PDOS thus derived are plotted in Fig. 3(a).

148 The obtained O  $2p$  PDOS is compared with the DOS  
 149 calculated by DFT (see Methods) in Fig. 3(b). One can  
 150 see good one-to-one correspondence between the exper-  
 151 imental and calculated structures in the O  $2p$  PDOS.  
 152 In particular, the assumed non-bonding O  $2p$ -band posi-  
 153 tion well agrees with the peak position of the calculated  
 154 non-bonding O  $2p$  band. Nevertheless, the conclusion of  
 155 the present paper will not be altered by the magnitude of  
 156 the band gap unless it collapses and the system becomes  
 157 metallic.

### 158 Low-energy multiplet and phonon satellites

159 In order to examine the effect of electron-phonon cou-  
 160 pling and possible low-symmetry crystal field, an en-  
 161 larged plot of the RIXS spectra in the low-energy region  
 162 is shown in Fig. 4(a). The “elastic” peak at  $E_{\text{loss}} = 0$  eV  
 163 is a superposition of the genuine elastic scattering (which  
 164 should be very weak for the present  $\pi$  scattering geome-  
 165 try) and low-energy (0–20 meV) elastic and quasi-elastic  
 166 scattering between the nearly degenerate five components  
 167 of the  $J_{\text{eff}} = 2$  ground state [see Fig. 1(b)]. The sharp  
 168 peak at  $E_{\text{loss}} \sim 0.4$  eV is due to excitation from the  $J_{\text{eff}} =$   
 169 2 ground state to the  $J_{\text{eff}} = 0$  and 1 excited states. The  
 170 latter excitation is also observed by Raman scattering as  
 171 described below. The weak peak at  $E_{\text{loss}} \sim 0.8$  eV is  
 172 an excited state of the  $t_{2g}^2$  multiplet having the quantum  
 173 number  $J_{\text{eff}} = 2$  [Fig. 1(b)]. Unfortunately, the residual  
 174 cubic splitting  $\Delta_c$  of the  $J_{\text{eff}} = 2$  state [Fig. 1(b)] is too  
 175 small to be resolved in the RIXS spectra. Each of the  
 176 quasi-elastic,  $E_{\text{loss}} \sim 0.4$  eV, and  $\sim 0.8$  eV peaks are  
 177 accompanied by sub-peaks with  $\sim 80$  meV intervals on  
 178 the higher-energy side. These sub-peaks are attributed  
 179 to phonon replicas, as described below.

### 180 Analyses using ligand-field multiplet theory

181 The magnitude of the SOC of the Os  $5d$  states can  
 182 be estimated from the O  $K$ -edge XAS [Fig. 2(a)]. X-ray  
 183 absorption into the empty  $t_{2g}$  state observed at 528–530  
 184 eV is split into double peaks separated by  $\frac{3}{2}\zeta \sim 0.7$  eV.  
 185 Note that for the effective angular momentum operator  
 186  $\mathbf{l}_{\text{eff}}$ , the SOC constant  $\zeta'$ , defined through the SOC en-  
 187 ergy  $\zeta' \mathbf{l}_{\text{eff}} \cdot \mathbf{s}$ , is given by  $\zeta' \equiv -\zeta$  because  $\mathbf{l}_{\text{eff}} \equiv -\mathbf{l}$  for the  
 188  $t_{2g}$  electrons [26], where  $\mathbf{l}$  is the bare angular momentum  
 189 operator. The cubic ligand-field (LF) splitting  $\Delta_{\text{LF}}$  of the  
 190 Os  $5d$  level into  $t_{2g}$  and  $e_g$  [Fig. 1(a)] can also be esti-  
 191 mated from the O  $K$ -edge XAS. From the broad absorp-  
 192 tion feature at 532–536 eV, the  $e_g$  component could be  
 193 isolated by monitoring the RIXS intensity of the  $J_{\text{eff}} = 2$   
 194 ( $t_{2g}^2$ )  $\rightarrow t_{2g}e_g$  energy-loss feature at  $E_{\text{loss}} \sim 5$  eV [marked

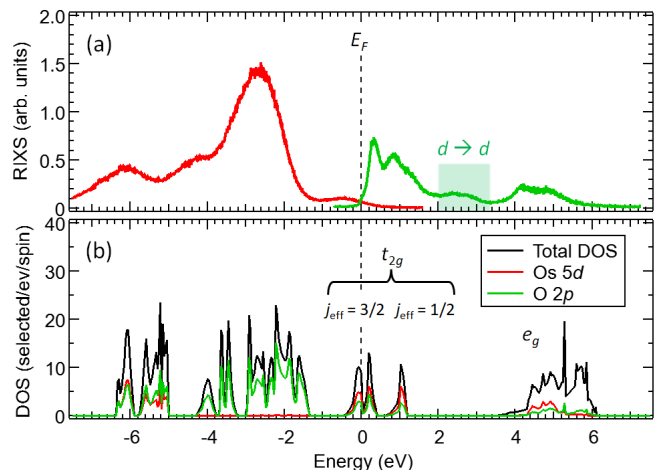


FIG. 3. O  $2p$  partial density of states (PDOS) derived from  
 experiment and theory. (a) Experimental O  $2p$  PDOS. The  
 empty part is derived from the O  $2p \rightarrow$  Os  $5d$  CT excitation  
 in the RIXS spectrum [ $E_{\text{in}} = 528.2$  eV,  $c$  in Fig. 2(d)], and the  
 occupied part from the fluorescence component of the RIXS  
 spectrum [ $E_{\text{in}} = 534.6$  eV,  $k$  in Fig. 2(d)]. The shaded part  
 marked by “ $d \rightarrow d$ ” arises from  $t_{2g}^2 \rightarrow t_{2g}e_g$  transition, and is  
 unrelated to the O  $2p$  PDOS. (b) PDOS of the nonmagnetic  
 state obtained by the GGA+ $U$ +SOC calculation with  $U -$   
 $J_H = 2.5$  eV.

195 by a solid line in Fig. 2(b)] as a function of  $E_{\text{in}}$ : Thus  
 196 obtained intensity plotted by the blue dashed curve at  
 197 the bottom of Fig. 2(a) gives the  $e_g$  component, allowing  
 198 us to obtain  $\Delta_{\text{LF}} \simeq 4$  eV.

199 To interpret the RIXS spectra quantitatively, LF mul-  
 200 tiplet calculations were performed and their results are  
 201 shown in Fig. 2(e). (For details, see Methods.) The cal-  
 202 culated  $d^2$  multiplet (red curves) reproduces the observed  
 203 loss peaks at  $E_{\text{loss}} \sim 0.4$  and  $0.8$  eV ( $t_{2g}^2$  part), and those  
 204 at  $E_{\text{loss}} \sim 4$  eV ( $t_{2g}e_g$  part). The RIXS spectra in the blue  
 205 shaded parts,  $E_{\text{loss}} \simeq 2$ –4 and 6–7 eV, cannot be repro-  
 206 duced by the  $d^2$  multiplet. We attribute these features to  
 207 O  $2p \rightarrow$  empty Os  $5d$  CT excitation, and simulate the CT  
 208 excitation spectrum by  $d^2 \rightarrow d^3$  multiplet calculation of  
 209 inverse-photoemission leaving a hole in the non-bonding  
 210 O  $2p$  band. By assuming that the non-bonding O  $2p$  band  
 211 is located  $\sim 2$  eV below  $E_F$ , as indicated by the DFT cal-  
 212 culation, and by ignoring the  $p$ -band width, we could re-  
 213 produce the CT spectrum from the  $J_{\text{eff}} = 2$  ground state  
 214 and plotted it by dashed blue curves in Fig. 2(e). The  
 215  $E_{\text{loss}} \simeq 2$ –4 eV region arises from O  $2p \rightarrow t_{2g}$  excitation  
 216 and the  $E_{\text{loss}} \simeq 6$ –7 eV region arises from O  $2p \rightarrow e_g$  CT  
 217 excitation.

218 Note that there are no features in the RIXS spectra  
 219 that indicate the lowering of the cubic symmetry: If the  
 220 LF symmetry were lower than the cubic one, the  $J_{\text{eff}} = 2$   
 221 ground state, which is split into the doublet  $E_g$  and the  
 222 triplet  $T_{2g}$  [Fig. 1(b)], would be further split into multiple  
 223 states as shown in Fig. 4(b) for cubic ( $O_h$ )-to-tetragonal  
 224 ( $D_{4h}$ ) symmetry lowering, and the low-energy part of the  
 225 RIXS spectra would be significantly different from the ex-

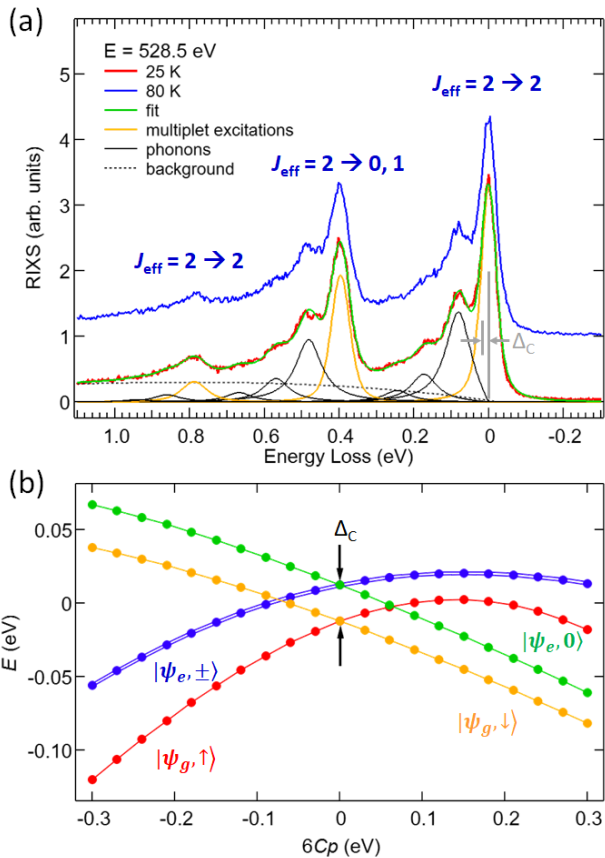


FIG. 4. Low-energy excitations measured by O  $K$ -edge RIXS.  $\Delta_c$  is the ‘residual’ cubic splitting of the  $J_{\text{eff}} = 2$  ground state defined in Fig. 1(b). (a) RIXS spectra in the low energy-loss region at different temperatures across the magnetic transition at  $T^* \sim 50$  K for the incident photon energy of 528.5 eV. The  $d$ - $d$  excitation shown in Fig. 1(b) is seen. The energy-loss peaks as well as the quasi-elastic peaks are accompanied by multiple phonon satellites. The splitting  $\Delta_c \sim 20$  meV is not resolved in the spectra. Details of the line-shape analysis are given in Supplementary Note 1 with Supplementary Figure 1 and Supplementary Table 1. (b) Energies of low-lying excited states of the  $\text{Os}^{6+}$  ( $5d^2$ ) ion as functions of the low-symmetry  $D_{4h}$  LF parameter  $6Cp$  [25], the splitting of the  $t_{2g}$  level. The  $O_h$  LF parameter  $\Delta_{\text{LF}}$  is set to 4.1 eV.  $|6Cp| \simeq 0.15$  reproduces the low-energy excitation in the O- $K$  RIXS spectra of the  $5d^1$  double perovskites [22, 23].

perimental ones in Fig. 4(a). If the tetragonal distortion were comparable to that of the  $5d^1$  double perovskites  $\text{Ba}_2\text{NaOsO}_6$  [22] and  $\text{Ba}_2\text{MgReO}_6$  [23], which show peak at  $E_{\text{loss}} \sim 0.1$  eV in the O  $K$ -edge RIXS spectra, the tetragonal crystal field  $6Cp$ , which is equal to the tetragonal splitting of the  $t_{2g}$  level [25] should be as large as  $\pm 0.15$  eV, and the quasi-elastic  $J_{\text{eff}} = 2 \rightarrow J_{\text{eff}} = 2$  peak would be split into a few peaks over an energy range of  $\sim 0.1$  eV in addition to the phonon satellites. The absence of temperature dependence in the spectral line shapes across the magnetic transition at  $T^* \sim 50$  K suggests that the magnetic transition does not involve any

appreciable structural change. Furthermore, there are no spectral features that can be attributed to magnons nor bi-magnons, consistent with the absence of spin order in  $\text{Ba}_2\text{CaOsO}_6$ .

The octupolar nature of the ground state of the  $\text{Os}^{6+}$  ion in the  $O_h$  field can be demonstrated by LF multiplet calculation with a weak magnetic field in the (1,1,1) direction as a time-reversal symmetry-breaking perturbation that splits the non-Kramers  $E_g$  doublet into  $|\psi_{g,+}\rangle$  and  $|\psi_{g,-}\rangle$ . For  $B = 10$  T, we obtained octupolar moment  $T_{xyz} \equiv \langle J^x J^y J^z \rangle \simeq 1.2$  with a tiny dipole magnetic moment of  $\sim 8 \times 10^{-3} \mu_B$  induced along the (1,1,1) direction on top of the octupolar ground state. For a smaller field of  $B = 1$  T, the induced dipolar moment was as small as  $\sim 7 \times 10^{-4} \mu_B$ . Generally, for a small field  $B \ll \Delta_c / \mu_B$ , the induced magnetic dipole moment along the direction of  $B$  ( $\sim \mu_B B / \Delta_c$ ) is proportional to  $B$ . While ordering with the finite magnetic octupolar or electric quadrupolar moment can occur within the  $E_g$  ground state, the appearance of a finite magnetic dipolar moment requires hybridization between the  $E_g$  and  $T_{2g}$  states. Thus, to obtain a stable magnetic dipole order by the exchange interaction, a molecular field of  $\mu_B B > \Delta_c$  at least is required.

### Phonon Raman scattering

To further confirm the absence of low-symmetry crystal field, we employed Raman scattering spectroscopy, a sensitive probe of lattice symmetry. Figure 5(a) shows one-phonon Raman spectra of a  $\text{Ba}_2\text{CaOsO}_6$  polycrystal taken at 80 K with two polarization geometries ( $\parallel$  and  $\perp$ ; for technical details, see Methods). There must be phonons of  $A_{1g} + E_g + T_{1g} + 2T_{2g} + 5T_{1u} + T_{2u}$  symmetries at the Brillouin-zone center in case of cubic  $\text{Fm}\bar{3}\text{m}$  structure, out of which four ( $A_{1g}$ ,  $E_g$ , and  $2T_{2g}$ ) phonons are Raman-active.

To obtain information about the symmetry of the observed excitation, polarization measurements were performed in two geometries - with parallel ( $\parallel$ ) and with mutually perpendicular ( $\perp$ ) polarizations of the incident and scattered light. We utilized the rules that in isotropic or cubic systems the depolarization ratio  $\rho = I_{\perp} / I_{\parallel}$  does not exceed 0.75 for totally symmetric modes, while it is close to 0.75 for non-totally symmetric ones [27]. One can see that the line at  $\sim 796.5 \text{ cm}^{-1}$  obviously dominates in the  $\parallel$  spectrum and can be assigned to the  $A_{1g}$  mode, while the phonons at frequencies 102.5, 375, and 495  $\text{cm}^{-1}$  are observed in both polarized  $\parallel$  and depolarized  $\perp$  spectra and are assigned to  $T_{2g}$ ,  $T_{2g}$ , and  $E_g$  modes, respectively, with the help of the non-magnetic DFT calculation of phonon modes as described in Supplementary Note 2 with Supplementary Figure 2. The broad peak at 720  $\text{cm}^{-1}$  has a fairly low depolarization ratio ( $\sim 0.2$ ), which suggests its  $A_{1g}$  symmetry. While its origin is not clear, the symmetry lowering cannot split the  $A_{1g}$  mode without the increase of the unit cell. (Note also that

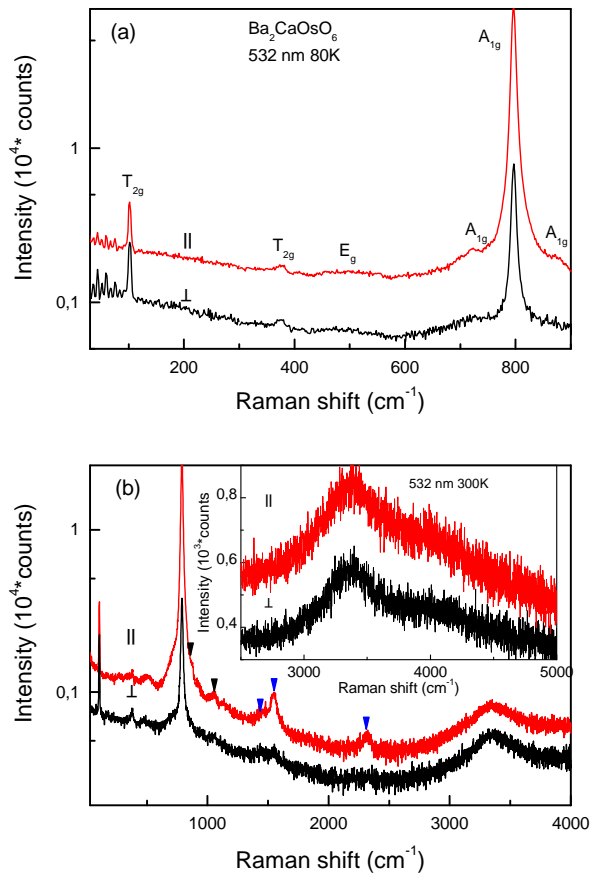


FIG. 5. Raman spectra in two scattering symmetries:  $\parallel$  (red) and  $\perp$  (black) are presented. (a) Frequency range with a one-phonon excitations. (b) Extended frequency range where the high-order phonon processes (blue arrows show features originating from the  $A_{1g}$  branch, black - another weak two-phonon features) and electronic excitation are seen. Latest are seen in the range from 3000 to 5000  $\text{cm}^{-1}$ , as shown in the inset, most probably due to the  $J_{\text{eff}} = 2 \rightarrow J_{\text{eff}} = 0, 1$  RIXS peaks (Fig. 4).

the second intensive  $T_{2g}$  mode remains unsplit.) The appearance of this low intensity  $A_{1g}$  peak can be, e.g., due to imperfections of the crystal structure (e.g. there are indications of anti-phase boundary defects with disorder at the  $B$  sites and other types of defects [28–31]) or a two-phonon repetition of  $375 \text{ cm}^{-1}$  vibration. Thus, our Raman experiments do not detect any direct evidence of the symmetry lowering in the cubic  $\text{Ba}_2\text{CaOsO}_6$ .

To examine the possible lattice distortions across  $T^* \sim 50 \text{ K}$ , we measured spectra at  $10 \text{ K}$  with better resolution and found only minor changes in the spectrum, such as further hardening and narrowing of the  $A_{1g}$  mode at  $\sim 796.5 \text{ cm}^{-1}$ . Interestingly, the frequency and unique line width of the low-frequency  $T_{2g}$  mode did not change in the whole temperature range of  $10\text{--}300 \text{ K}$ .

The higher frequency range from  $800$  to  $3000 \text{ cm}^{-1}$  presented in Fig. 5(b) shows several peaks dominating in the  $\parallel$  geometry and hence of the  $A_{1g}$  symmetry. The weak

peaks at  $870$  and  $1055 \text{ cm}^{-1}$  indicated by black arrows are probably two-phonon features. The peaks at  $1450$ ,  $1540$  and  $2310 \text{ cm}^{-1}$  shown by blue arrows can be associated with double and triple phonon scattering from the  $A_{1g}$  phonon branch. At higher frequencies ( $>3000 \text{ cm}^{-1}$ ), two broad peaks are observed. They are clearly seen in both polarization geometries ( $\parallel$  and  $\perp$ ), as well as upon excitation by both used laser lines ( $532$  and  $633 \text{ nm}$ , see Methods), which indicates Raman scattering by electron excitations of  $T_{2g}$  or  $E_g$  symmetry. Their energies agree well with the  $J_{\text{eff}} = 2 \rightarrow J_{\text{eff}} = 0, 1$  RIXS peaks (Fig. 4).

Typically, in the case of  $5d^2$  double perovskites, the effect of tetragonal distortions on the ground state is considered due to their stronger coupling with electronic structure [32]. Interestingly, Rayyan *et al.* [33] included the trigonal distortions in their analysis and demonstrated that, while these distortions are unable to split the  $E_g$  doublet due to symmetry constraints, they can lift the degeneracy of the higher-lying  $T_{2g}$  triplet. Under trigonal distortions, some of these  $T_{2g}$  states go to a lower energy. However, as shown in [33] there is a rather wide range of trigonal distortion under which the non-Kramers  $E_g$  doublet remains the ground state. This doublet may, therefore, survive as the ground state under a small lattice distortion. It is also possible that distortion is substantially reduced due to dynamical Jahn-Teller effect. Whether the  $E_g$  doublet hosts an electric quadrupole or a magnetic octupole or both depends on the type of broken symmetry (spatial symmetry or time-reversal symmetry) and the strength of the mean field from neighboring Os ions.

### Electron-phonon coupling effects on RIXS

In the low-energy RIXS spectra shown in Fig. 4, the quasi-elastic peak and the peak at  $E_{\text{loss}} \simeq 0.4 \text{ eV}$  are accompanied by sub-peaks separated by  $\sim 80$ ,  $160$ , and  $240 \text{ meV}$  with decreasing intensities. We attribute the sub-peaks to phonon replicas created by the simultaneous excitation of optical phonons. The one-phonon energy of  $\sim 80 \text{ meV}$  is somewhat lower but in a similar range as the Raman  $A_{1g}$  mode energies  $720 \text{ cm}^{-1} = 88 \text{ meV}$  and  $796.5 \text{ cm}^{-1} = 99 \text{ meV}$ . The replica energies are close to those observed in the RIXS spectra of  $\text{Ba}_2\text{NaOsO}_6$  [22]. From the replica intensities, the dimensionless electron-phonon coupling constant is estimated to be  $M/\omega_0 \gtrsim 1$ , where  $M$  is the average electron-phonon coupling matrix element and  $\omega_0$  is the phonon energy [34]. In spite of the moderately strong coupling, Jahn-Teller distortion is suppressed in  $\text{Ba}_2\text{CaOsO}_6$  due to the strong SOC and dynamical Jahn-Teller effect, suggesting that Os-Os exchange interaction is strong enough to stabilize the magnetic octupole over the electric quadrupole. Here, it should be noted that sub-peaks similar to the phonon replicas may appear in the RIXS spectra if dynamical Jahn-Teller effect [35] exists, as reported for the  $5d^1$  sys-

TABLE I. Parameter values for the Os  $5d$  electrons hybridized with O  $2p$  orbitals in  $\text{Ba}_2\text{CaOsO}_6$  derived in the present XAS and RIXS spectra.

Parameter	Symbol	Value (eV)
ligand-field splitting	$\Delta_{\text{LF}}$	4.1
Spin-orbit coupling for the $5d$ shell	$\zeta$	0.47
Spin-orbit coupling for the $t_{2g}$ shell	$\zeta'$	-0.47
Hund's coupling for the $t_{2g}$ shell	$J_{\text{H}}$	0.27

tem  $\text{Ba}_2\text{CaReO}_6$  [18, 19]. Whether such an effect also exists in  $5d^2$  systems or not is an interesting question to be pursued in future studies. Considering the different time scales of RIXS (on the order of 0.01 fs) and Raman scattering ( $> 10$  fs), it is possible that dynamical Jahn-Teller effect was seen in RIXS as the ‘‘phonon replicas’’ but not in Raman scattering.

### III. DISCUSSION

We have investigated the electronic structure of  $\text{Ba}_2\text{CaOsO}_6$  by XAS, RIXS, and Raman scattering experiment as well as DFT calculation, focusing on extracting reliable parameters characterizing the systems, as summarized in Table I, and on the confirmation of the local cubic symmetry of the Os ions that favors the octupolar state as the origin of its ‘hidden order’. We have also confirmed the octupolar nature of the non-Kramers  $E_g$  doublet ground state ( $|S_z| = 0$  and  $|L_z| = 0$  under an infinitesimally small magnetic field) by LF multiplet calculation.

Owing to the hybridization between the O  $2p$  and Os  $5d$  orbitals, electronic excitation within the  $5d^2$  multiplet and charge-transfer excitation from the occupied O  $2p$  to the empty Os  $5d$  states could be identified by the O  $K$ -edge RIXS. From comparison of the XAS and RIXS line shapes with the LF multiplet calculation, the absence of splitting of low-energy RIXS peaks as well as the lack of additional lines in Raman scattering spectra we conclude that no crystal field lower than the cubic one can be identified, consistent with the small ( $\sim 20$  meV) residual cubic splitting of the  $J_{\text{eff}} = 2$  ground state. The present results obtained by different types of X-ray and optical spectroscopy, which are typically very sensitive to a local environment of transition metals, substantially strengthen previous findings, in particular diffraction data demonstrating the absence of non-cubic distortions [14].

There are two possible mechanisms working hand-in-hand in suppressing the Jahn-Teller distortion expected for the  $\text{Os}^{6+}$  ion with the  $d^2$  configuration. In both mechanisms, the strong SOC is involved. One is an on-site effect related to the stabilization of electrons not at cubic harmonics as the crystal field (i.e. Jahn-Teller effect) would prefer, but rather on entangled spin-orbitals [4, 36]. Our RIXS measurements clearly resolved phonon replicas of the  $J_{\text{eff}} = 2 \rightarrow 1, 0, 2$  excitation peaks.

This allowed us to estimate the electron-phonon coupling strength, which turns out to be moderately strong,  $M/\omega_0 \gtrsim 1$  and, therefore, may not be sufficiently strong to recover the Jahn-Teller distortion but might induce dynamical Jahn-Teller effect. On the other hand, there is also inter-site effect – the energy gain due to exchange interaction between the octupoles, which are formed by SOC. Further spectroscopic and theoretical studies are necessary to identify the octupolar order and its microscopic origin.

## METHODS

### Materials preparation

Polycrystalline  $\text{Ba}_2\text{CaOsO}_6$  was synthesized through a solid-state reaction using fine powders of  $\text{BaO}_2$  (99% purity, Kojundo Chemical Laboratory Co., Ltd.),  $\text{CaO}_2$  (prepared in the laboratory [37]), and Os (99.95% purity, Nanjing Dongrui Platinum Co. Ltd.) in a ratio of 2:1:1.1. Approximately 200 mg of the mixed materials were placed into an alumina crucible. The mixture was then heated in air to  $1000^\circ\text{C}$  for 7 hours, followed by a 1-hour dwell time, and subsequent cooling to room temperature over a span of 7 hours. After re-mixing and pressing, the sample was annealed at  $1000^\circ\text{C}$  for 24 hours. The resulting product is a grey sintered pellet, possessing sufficient solidity to be manipulated with tweezers. Powder X-ray diffraction analysis was performed using Cu  $K\alpha$  radiation within the  $5^\circ \leq 2\theta \leq 65^\circ$  range at 293 K. The measurements were conducted with a MiniFlex600 diffractometer (Rigaku, Tokyo, Japan). The acquired data, shown in Supplementary Figure 3, exhibited good agreement with simulations based on the crystallographic data of  $\text{Ba}_2\text{CaOsO}_6$  [12], confirming the single-phase nature of the product.

### Resonant inelastic X-ray scattering

All resonant inelastic X-ray scattering (RIXS) and X-ray absorption spectroscopy (XAS) measurements at the O  $K$  edge were performed using the AGM-AGS spectrometer of beamline 41A at Taiwan Photon Source of National Synchrotron Radiation Research Center (NSRRC) [38]. This beamline is based on the energy compensation principle of grating dispersion [39]. The energy bandwidth of incident X-ray was 0.2 eV (0.1 eV for XAS measurement) while keeping the total energy resolution of RIXS as 30 meV at the incident photon energy of 528.5 eV. The sample surface was cleaned by scraping with a diamond file in the Ar glove box before the measurement and was transferred into the measurement chamber without exposure to the air. The base pressure of the measurement chamber was  $\leq 1 \times 10^{-8}$  Torr. The sample was cooled down to 25 K with liquid helium during the measurements. Both RIXS and XAS

461 measurements were carried out using linear horizontally  
 462 ( $\pi$ ) polarized X-rays. The XAS spectra were measured  
 463 with a normal-incident X-ray in the total fluorescence  
 464 yield mode. For the RIXS measurement, the incidence  
 465 angle was fixed at  $20^\circ$ , and the scattering angle was fixed  
 466 at  $90^\circ$ . The combination of the  $\pi$ -polarized X-rays and  
 467 the  $90^\circ$  scattering angle makes the RIXS signals purely  
 468 magnetic. The same geometry also allowed us to reduce  
 469 the elastic peak and to study low-energy excitation effec-  
 470 tively.

### 471 Ligand-field multiplet calculation

472 Ligand-field multiplet (LF) calculations were per-  
 473 formed by using the XTLS 8.5 package [40]. In the calcu-  
 474 lation of the O  $K$ -edge RIXS spectra, we assumed that  
 475 the excited states of the  $5d^2$  multiplet can be reached  
 476 by O  $K$ -edge RIXS through the strong Os  $5d$ -O  $2p$  hy-  
 477 bridization and could be simulated by the calculation of  
 478 Os  $L_{2,3}$ -edge RIXS by setting the  $2p$ - $5d$  Slater integrals  
 479 and the Os  $2p$  core-level SOC to zero. While this simu-  
 480 lation would give the energy positions of RIXS features  
 481 correctly, it would not give correct intensities because  
 482 relevant transition-matrix elements are not used. The  
 483 O  $K$ -edge XAS [Fig. 2(a)] was also simulated by the Os  
 484  $L_{2,3}$ -edge XAS in the same manner.

485 In general, the Slater integrals  $F$ 's and  $G$ 's (anisotropy  
 486 of Coulomb interaction) and the SOC coupling constant  
 487  $\zeta$  in solids are smaller than those of isolated atoms, be-  
 488 cause the wavefunctions are more spatially extended due  
 489 to hybridization. In order to model this effect, the atomic  
 490 Slater integrals and  $\zeta$ , deduced from Hartree-Fock cal-  
 491 culations [41, 42], were multiplied by constant factors  
 492  $R_{\text{Slater}}$  and  $R_{\text{SOC}}$  ( $0 \leq R_{\text{Slater}} < 1$ ,  $0 \leq R_{\text{SOC}} < 1$ ),  
 493 respectively. These factors  $R_{\text{Slater}}$  and  $R_{\text{SOC}}$  and the  
 494 cubic LF splitting  $\Delta_{\text{LF}}$  and were treated as adjustable  
 495 parameters. For O  $K$ -edge RIXS,  $\zeta = 0.50$  eV and  
 496  $\Delta_{\text{LF}} = 4.1$  eV were used, and the Slater integrals be-  
 497 tween the Os  $5d$  orbitals were reduced to 35% of the  
 498 atomic Hartree-Fock values. Hund's coupling  $J_{\text{H}}$  between  
 499 two  $d$  electrons (Table I) is related to Slater integrals  
 500 through  $J_{\text{H}} = \frac{3}{49}F^2 + \frac{20}{441}F^4$  [43]. The value  $J_{\text{H}} = 0.27$   
 501 eV in the table is smaller than  $J_{\text{H}} = 0.5$  eV used for the  
 502 DFT+ $U$ +SOC calculation because the former is for the  
 503 Os  $5d$ -O  $2p$  anti-bonding orbitals while the latter for the  
 504 Os  $5d$  atomic orbitals. The reduction of  $J_{\text{H}}$  from 0.5 eV  
 505 to 0.27 eV suggests that the atomic orbitals consisting of  
 506 the antibonding  $t_{2g}$  band have the weight Os  $5d$ : O  $2p \sim$   
 507 70%: 30%.

508 In the calculation of the RIXS spectra, the same geom-  
 509 etry as the experiment was adopted: The incident and  
 510 scattered X-rays were set parallel to the cubic [001] and  
 511 [100] directions, respectively. Taking the [001], [100], and  
 512 [010] directions as the  $z$ ,  $x$ ,  $y$  axes, respectively, the linear  
 513 polarizations of the incident and scattered X-rays were  
 514 set to be  $(x, y)$  and  $(x, z)$ , and the spectra for these two  
 515 polarization sets were averaged.

516 The calculated spectra were broadened by a Voigt func-  
 517 tion, which is the convolution of a Lorentz function and  
 518 a Gauss function. The widths (half width at half maxi-  
 519 mum, HWHM) of the Lorentz functions were determined  
 520 from the natural lifetime of the core holes: 0.05 eV for  
 521 the O  $K$ -edge RIXS [44]. The widths (standard devia-  
 522 tion) of the Gauss functions were assumed to be 0.01 eV.  
 523 The XAS and RIXS spectra were calculated for the five  
 524 lowest states [the lowest  $J_{\text{eff}} = 2$  state in Fig. 1(b)] as  
 525 the initial state and were summed up according to the  
 526 Boltzmann distribution of the initial states.

### 527 Raman spectroscopy

528 Raman measurements in the 10-300K range were per-  
 529 formed in backscattering geometry from the polycryst-  
 530 talline sample using an RM1000 Renishaw microspector-  
 531 ometer equipped with a 532 nm solid-state laser and  
 532 633 helium-neon laser. Very low power (up to 1 mW)  
 533 was used to avoid local heating of the sample. A pair of  
 534 notch filters with a cut-off at  $60 \text{ cm}^{-1}$  were used to sup-  
 535 press light from the 633 nm laser line. To reach as close  
 536 to the zero frequency as possible, we used a set of three  
 537 volume Bragg gratings (VBG) at 532 nm excitation to  
 538 analyze the scattered light. The resolution of our Raman  
 539 spectrometer was estimated to be  $2\text{-}3 \text{ cm}^{-1}$ .

540 The temperature dependence of the two narrow lines in  
 541 the spectrum [Fig. 5 (a)] turned out to be opposite. The  
 542 fully symmetric line softened from  $797.5$  to  $788.5 \text{ cm}^{-1}$   
 543 with an increase in the temperature range from 10 to 300  
 544 K, and its width increased from  $6.5$  to  $12 \text{ cm}^{-1}$ , which  
 545 can be explained by anharmonicity effects. In contrast to  
 546 this behavior, the energy and width of the low-frequency  
 547  $T_{2g}$  phonon line remains constant within the measure-  
 548 ment error ( $\omega \sim 102.5 \text{ cm}^{-1}$  and  $\Gamma \sim 1.5 \text{ cm}^{-1}$ ) when  
 549 heated from 10 to 300 K. Unfortunately, the tempera-  
 550 ture behavior of the two broad lines -  $T_{2g}$  at  $375 \text{ cm}^{-1}$   
 551 ( $\Gamma \sim 20 \text{ cm}^{-1}$ ) and  $E_g$  at  $495 \text{ cm}^{-1}$  ( $\Gamma \sim 60 \text{ cm}^{-1}$ ) - is  
 552 difficult to study due to their weak intensity. However,  
 553 despite the large width of the lines, we did not find any  
 554 signs of their splitting.

### 555 Density-functional-theory calculation

556 The generalized gradient approximation (GGA) in the  
 557 form proposed by Perdew, Burke, and Ernzerhof [45]  
 558 as realized in VASP code [46] was used for the density  
 559 functional theory calculations. Phonon spectra shown in  
 560 Supplementary Figure 2 were calculated by the frozen  
 561 phonon method [47] with  $5 \times 5 \times 5$  mesh of the Brill-  
 562 ouin zone of the  $2 \times 2 \times 2$  supercell in non-magnetic  
 563 GGA. Planewave cut-off was set up to 500 eV. The struc-  
 564 ture was relaxed until convergence in energy of  $10^{-6}$  eV  
 565 in electronic subsystem and  $10^{-5}$  eV in ionic one was  
 566 achieved.

568 All data generated or analysed during this study are  
569 available from the corresponding authors upon reason-  
570 able request.

- 
- 571 [1] T. Takayama, J. Chaloupka, A. Smerald, G. Khaliullin, 625  
572 and H. Takagi, Spin-orbit-entangled electronic phases in 626  
573  $4d$  and  $5d$  transition-metal compounds, *J. Phys. Soc. Jpn* 627  
574 **90**, 062001 (2021). 628
- 575 [2] D. I. Khomskii and S. V. Streltsov, Orbital effects in 629  
576 solids: Basics, recent progress, and opportunities, *Chem.* 630  
577 *Rev.* **121**, 2992 (2021). 631
- 578 [3] D. I. Khomskii and S. V. Streltsov, Magnetic oxides, in 632  
579 *Encyclopedia of Condensed Matter Physics (Second Edition)*, 633  
580 edited by T. Chakraborty (Academic Press, Oxford, 2024) 634  
581 second edition ed., pp. 98–111. 635
- 582 [4] S. V. Streltsov and D. I. Khomskii, Jahn-Teller effect and 636  
583 spin-orbit coupling: Friends or foes?, *Phys. Rev. X* **10**, 637  
584 031043 (2020). 638
- 585 [5] G. Chen and L. Balents, Spin-orbit coupling in  $d^2$  ordered 639  
586 double perovskites, *Phys. Rev. B* **84**, 094420 (2011). 640
- 587 [6] A. Paramekanti, D. D. Maharaj, and B. D. Gaulin, Octu- 641  
588 pular order in  $d$ -orbital Mott insulators, *Phys. Rev. B* 642  
589 **101**, 054439 (2020). 643
- 590 [7] C. Svoboda, W. Zhang, M. Randeria, and N. Trivedi, 644  
591 Orbital order drives magnetic order in  $5d^1$  and  $5d^2$  double 645  
592 perovskite Mott insulators, *Phys. Rev. B* **104**, 024437 646  
593 (2020). 647
- 594 [8] G. Khaliullin, D. Churchill, P. P. Stavropoulos, and H.- 648  
595 Y. Kee, Exchange interactions, Jahn-Teller coupling, and 649  
596 multipole orders in pseudospin one-half  $5d^2$  Mott insula- 650  
597 tors, *Phys. Rev. Res.* **3**, 033163 (2021). 651
- 598 [9] S. Voleti, K. Pradhan, S. Bhattacharjee, T. Saha- 652  
599 Dasgupta, and A. Paramekanti, Probing octupolar hidden 653  
600 order via janus impurities, *npj Quantum Mater.* **8**, 654  
601 42 (2023). 655
- 602 [10] D. Hirai, H. Sagayama, S. Gao, H. Ohsumi, G. Chen, 656  
603 T. Arima, , and Z. Hiroi, Detection of multipolar orders 657  
604 in the spin-orbit-coupled  $5d$  Mott insulator  $\text{Ba}_2\text{MgReO}_6$ , 658  
605 *Phys. Rev. Res.* **2**, 022063(R) (2020). 659
- 606 [11] A. Takahashi and H. Shiba, Possible orbital orderings 660  
607 in a model of metallic double-exchange ferromagnets, *J.* 661  
608 *Phys. Soc. Jpn.* **69**, 3328 (2000). 662
- 609 [12] C. M. Thompson, J. P. Carlo, R. Flacau, T. Aharen, 663  
610 I. A. Leahy, J. R. Pollicemi, T. J. S. Munsie, T. Medina, 664  
611 G. M. Luke, J. Munevar, S. Cheung, T. Goko, Y. J. Ue- 665  
612 mura, and J. E. Greedan, Long-range magnetic order in 666  
613 the  $5d^2$  double perovskite  $\text{Ba}_2\text{CaOsO}_6$ : comparison with 667  
614 spin-disordered  $\text{Ba}_2\text{YReO}_6$ , *J. Phys.: Condens. Matter* 668  
615 **26**, 306003 (2014). 669
- 616 [13] R. Cong, E. Garcia, P. C. Forino, A. Tasseti, G. Al- 670  
617 lodi, A. P. Reyes, P. M. T. P. M. Woodward, C. Franchi- 671  
618 nini, S. Sanna, and V. F. Mitrović, Effects of charge 672  
619 doping on mott insulator with strong spin-orbit coupling, 673  
620  $\text{Ba}_2\text{Na}_{1-x}\text{Ca}_x\text{OsO}_6$ , *Phy. Rev. Mater.* **7**, 084409 (2023). 674
- 621 [14] D. D. Maharaj, G. Sala, M. B. Stone, E. Kermarrec, 675  
622 C. Ritter, F. Fauth, C. A. Marjerrison, J. E. Greedan, 676  
623 A. Paramekanti, and B. D. Gaulin, Octupolar versus Néel 677  
624 order in cubic  $5d^2$  double perovskites, *Phys. Rev. Lett.* 678  
**124**, 087206 (2020).
- [15] S. Voleti, D. D. Maharaj, B. D. Gaulin, G. Luke, and 679  
A. Paramekanti, Multipolar magnetism in  $d$ -orbital sys- 680  
tems: Crystal field levels, octupolar order, and orbital 681  
loop currents, *Phys. Rev. B* **101**, 155118 (2020). 682
- [16] D. G. Mazzone, Y. Shen, H. Suwa, G. Fabbris, J. Yang, 683  
S.-S. Zhang, H. Miao, J. Sears, K. Jia, Y. G. Shi, M. H. 684  
Upton, D. M. Casa, X. Liu, J. Liu, C. D. Batista, and 685  
M. P. M. Dean, Antiferromagnetic excitonic insulator 686  
state in  $\text{Sr}_3\text{Ir}_2\text{O}_7$ , *Nat. Commun.* **13**, 913 (2022). 687
- [17] B. W. Lebert, S. Kim, B. H. Kim, S. H. Chun, D. Casa, 688  
J. Choi, S. Agrestini, K. Zhou, M. Garcia-Fernandez, and 689  
Y.-J. Kim, Nonlocal features of the spin-orbit exciton in 690  
Kitaev materials, *Phys. Rev. B* **108**, 155122 (2023). 691
- [18] F. I. Frontini, G. H. Johnstone, N. Iwahara, P. Bhat- 692  
tacharyya, N. A. Bogdanov, L. Hozoi, M. H. Upton, 693  
D. M. Casa, D. Hirai, , and Y.-J. Kim, Spin-orbit-lattice 694  
entangled state in  $\text{A}_2\text{MgReO}_6$  ( $\text{A} = \text{Ca}, \text{Sr}, \text{Ba}$ ) revealed 695  
by resonant inelastic X-ray scattering, *Phys. Rev. Lett.* 696  
**133**, 036501 (2024). 697
- [19] N. Iwahara, J.-R. Soh, D. Hirai, I. Živković, Y. Wei, 698  
W. Zhang, C. Galdino, T. Yu, K. Ishii, F. Pisani, 699  
O. Malanyuk, T. Schmitt, and H. M. Rønnow, Persistent 700  
quantum vibronic dynamics in a  $5d^1$  double perovskite 701  
oxide, arXiv:2409.08095 (2024). 702
- [20] X. Lu, P. Olalde-Velasco, Y. Huang, V. Bisogni, J. Pel- 703  
licciari, S. Fatale, M. Dantz, J. G. Vale, E. C. Hunter, 704  
J. Chang, V. N. Strocov, R. S. Perry, M. Grioni, D. F. 705  
McMorrow, H. M. Rønnow, and T. Schmitt, Dispersive 706  
magnetic and electronic excitations in iridate perovskites 707  
probed by oxygen  $K$ -edge resonant inelastic x-ray scat- 708  
tering, *Phys. Rev. B* **97**, 041102(R) (2018).
- [21] M. M. Sala, M. Rossi, S. Boseggia, J. Akimitsu, N. B. 709  
Brookes, M. Isobe, M. Minola, H. Okabe, H. M. Rønnow, 710  
L. Simonelli, D. F. McMorrow, and G. Monaco, Orbital 711  
occupancies and the putative  $j_{\text{eff}} = 1/2$  ground state in 712  
 $\text{Ba}_2\text{IrO}_4$ : A combined oxygen  $K$ -edge XAS and RIXS 713  
study, *Phys. Rev. B* **89**, 121101(R) (2014). 714
- [22] S. Agrestini, F. Borgatti, P. Florio, J. Frassinetti, D. F. 715  
Mosca, Q. Faure, B. Detlefs, C. J. Sahle, S. Fran- 716  
coua, J. Choi, M. Garcia-Fernandez, K.-J. Zhou, V. F. 717  
Mitrović, P. M. Woodward, G. Ghiringhelli, C. Franchini, 718  
F. Boscherini, S. Sanna, and M. M. Sala, Origin of mag- 719  
netism in a supposedly nonmagnetic osmium oxide, *Phys.* 720  
*Rev. Lett.* **133**, 066501 (2024). 721
- [23] I. Živković, J.-R. Soh, O. Malanyuk, R. Yadav, F. Pisani, 722  
A. M. Tehrani, D. Tolj, J. Pasztorova, D. Hirai, YuanWei, 723  
W. Zhang, C. Galdino, T. Yu, K. Ishii, A. Demuer, O. V. 724  
Yazyev, T. Schmitt, and H. M. Rønnow, Dynamic Jahn- 725  
Teller effect in the strong spin-orbit coupling regime, *Nat.* 726  
*Commun.* **15**, 8587 (2024). 727
- [24] V. Zimmermann, A. K. Yogi, D. Wong, C. Schulz, 728  
M. Bartkowiak, K. Habicht, L. Wang, M. Isobe, M. Mi- 729  
nola, G. Khaliullin, B. Keimer, and M. Hepting, Coherent 730

- propagation of spin-orbit excitons in a correlated metal, npj Quantum Mater. **8**, 53 (2023).
- [25] G. van der Laan, R. Chopdekar, Y. Suzuki, and E. Arenholz, Strain-induced changes in the electronic structure of  $\text{MnCr}_2\text{O}_4$  thin films probed by x-ray magnetic circular dichroism, Phys. Rev. Lett. **105**, 067405 (2010).
- [26] J. Kanamori, Theory of the magnetic properties of ferrous and cobaltous oxides I, Prog. Theor. Phys. **17**, 177 (1957).
- [27] D. P. Strommen, Specific values of the depolarization ratio in Raman spectroscopy: Their origins and significance, J. Chem. Educ. **69**, 803 (1992).
- [28] P. Woodward, R. Hoffmann, and A. Sleight, Order-disorder in  $A_2M^{3+}M^{5+}\text{O}_6$  perovskites, J. Mater. Res. **9**, 2118 (1994).
- [29] V. Ting, Y. Liu, R. Withers, L. Norén, M. James, and J. F. Gerald, A structure and phase analysis investigation of the “1:1” ordered  $A_2\text{InNbO}_6$  perovskites ( $A = \text{Ca}^{2+}$ ,  $\text{Sr}^{2+}$ ,  $\text{Ba}^{2+}$ ), J. Solid State Chem. **179**, 551 (2006).
- [30] C. Bernuy-Lopez, M. Allix, C. A. Bridges, J. B. Claridge, and M. J. Rosseinsky,  $\text{Sr}_2\text{MgMoO}_{6-\delta}$ : structure, phase stability, and cation site order control of reduction, Chem. Mat. **19**, 1035 (2007).
- [31] S. Vasala and M. Karppinen,  $A_2B'B''\text{O}_6$  perovskites: A review, Prog. Solid State Chem. **43**, 1 (2015).
- [32] I. B. Bersuker, *The Jahn-Teller Effect* (Cambridge University Press, Cambridge, 2006).
- [33] A. Rayyan, X. Liu, and H.-Y. Kee, Fate of multipolar physics in  $5d^2$  double perovskites, Phy. Rev. B **108**, 045149 (2023).
- [34] L. J. P. Ament, M. van Veenendaal, and J. van den Brink, Determining the electron-phonon coupling strength from resonant inelastic X-ray scattering at transition metal  $L$ -edges, Europhys. Lett. **95**, 27008 (2011).
- [35] N. Iwahara and W. Furukawa, Vibronic effect on resonant inelastic x-ray scattering in cubic iridium hexahalides, Phys. Rev. B **108**, 075136 (2023).
- [36] S. V. Streltsov, F. V. Temnikov, K. I. Kugel, and D. I. Khomskii, Interplay of the Jahn-Teller effect and spin-orbit coupling: The case of trigonal vibrations, Phys. Rev. B **105**, 205142 (2022).
- [37] Y. Shi, Y. Guo, S. Yu, M. Arai, A. Sato, A. A. Belik, K. Yamaura, and E. Takayama-Muromachi, Crystal growth and structure and magnetic properties of the  $5d$  oxide  $\text{Ca}_3\text{LiOsO}_6$ : extended superexchange magnetic interaction in oxide, J. Am. Chem. Soc. **132**, 8474 (2010).
- [38] A. Singh, H. Y. Huang, Y. Y. Chu, C. Y. Hua, S. W. Lin, H. S. Fung, H. W. Shiu, J. Chang, J. H. Li, J. Okamoto, C. C. Chiu, C. H. Chang, W. B. Wu, S. Y. Perng, S. C. Chung, K. Y. Kao, S. C. Yeh, H. Y. Chao, J. H. Chen, D. J. H. Huang, and C. T. Chen, Development of the Soft X-ray AGM-AGS RIXS beamline at the Taiwan Photon Source, J. Synchrotron Rad. **28**, 977 (2021).
- [39] C. H. Lai, H. S. Fung, W. B. Wu, H. Y. Huang, H. W. Fu, S. W. Lin, S. W. Huang, C. C. Chiu, D. J. Wang, L. J. Huang, T. C. Tseng, S. C. Chung, C. T. Chen, and D. J. Huang, Highly efficient beamline and spectrometer for inelastic soft x-ray scattering at high resolution, J. Synchrotron Rad. **21**, 325 (2014).
- [40] A. Tanaka and T. Jo, Resonant  $3d$ ,  $3p$  and  $3s$  photoemission in transition metal oxides predicted at  $2p$  threshold, J. Phys. Soc. Jpn. **63**, 2788 (1994).
- [41] J. B. Mann, *Atomic Structure Calculations. I. Hartree-Fock Energy Results for the Elements Hydrogen to Lawrencium*, Tech. Rep. (Los Alamos National Lab., Los Alamos, New Mexico, 1967).
- [42] F. Herman and S. Skillman, Atomic structure calculations, in *Atomic Structure Calculations* (Prentice-Hall Inc., Englewood Cliffs, New Jersey, 1963) Chap. 2, pp. 1–17.
- [43] A. Georges, L. de’ Medici, and J. Mravlje, Strong correlations from Hund’s coupling, Annu. Rev. Condens. Matter Phys. **4**, 137 (2013).
- [44] M. O. Krause and J. H. Oliver, Natural widths of atomic  $K$  and  $L$  levels,  $K\alpha$  X-ray lines and several  $KLL$  Auger lines, J. Phys. Chem. Ref. Data **8**, 329 (1979).
- [45] J. P. Perdew, K. Burke, and M. Ernzerhof, Generalized gradient approximation made simple, Phys. Rev. Lett. **77**, 3865 (1996).
- [46] G. Kresse and J. Furthmüller, Efficient iterative schemes for *ab initio* total-energy calculations using a plane-wave basis set, Phys. Rev. B **54**, 11169 (1996).
- [47] A. Togo, First-principles phonon calculations with phonopy and phono3py, J. Phys. Soc. Jpn. **92**, 012001 (2023).

## ACKNOWLEDGEMENTS

We are grateful to M. Haverkort, A. Paramekanti, C. Franchini, and A. Hariki for useful discussions. The soft X-ray measurements were conducted at beam line 41A of Taiwan Photon Source. This work was partly supported by the National Science and Technology Council of Taiwan under Grant Nos. 103-2112-M-213-008-MY3, 108-2923-M-548 213-001, and 113-2112-M-007-033 and by the Japan Society for the Promotion of Science under Grant Nos. JP20K14416 and JP22K03535. We thank the Ministry of Science and Higher Education of the Russian Federation for supporting Raman experiments and their interpretation through funding the Institute of Metal Physics, while theoretical calculations were performed with aid of the Russian Science Foundation (project RSF 23-42-00069). A.F. acknowledges the support from the Yushan Fellow Program under the Ministry of Education of Taiwan.

## AUTHOR CONTRIBUTIONS

A.F., S.V.S. and D.J.H. coordinated the project. J.O., H.Y.H., A.S., D.J.H. and C.T.C. developed the RIXS instruments and conducted the RIXS experiments. Y.S.P. performed Raman experiments. H.H. and K.Y. synthesized and characterized the sample. G.S. and A.T. performed multiplet calculations. J.O., D.J.H., S.V.S. and A.F. analyzed the data and wrote the paper with inputs from other authors.

## COMPETING INTERESTS

The authors declare that there are no competing interests.